



Cr₂O₃ scale growth rates on metallic interconnectors derived from 40,000 h solid oxide fuel cell stack operation



Markus Linder ^{a,*}, Thomas Hocker ^a, Lorenz Holzer ^a, K. Andreas Friedrich ^b, Boris Iwanschitz ^c, Andreas Mai ^c, J. Andreas Schuler ^c

^a Institute of Computational Physics, ZHAW Zurich University of Appl. Sciences, Technikumstrasse 9, CH-8401 Winterthur, Switzerland

^b Deutsches Zentrum für Luft- und Raumfahrt, Institut für Technische Thermodynamik, Pfaffenwaldring 38-40, D-70569 Stuttgart, Germany

^c Hexis AG, ZumPark 5, CH-8404 Winterthur, Switzerland

HIGHLIGHTS

- Cr₂O₃ formation is analyzed on interconnect post-test samples operated for 40,000 h.
- Cr₂O₃ growth rate is twice as fast on anode side in comparison to cathode side.
- Dedicated image processing method is applied for a reliable Cr₂O₃ quantification.
- Cr₂O₃ microstructure is affected by fuel variation along fuel supply channels.
- Description of Cr₂O₃ scale growth by Wagner's parabolic law is not suited in general.

ARTICLE INFO

Article history:

Received 28 January 2013

Received in revised form

21 May 2013

Accepted 29 May 2013

Available online 14 June 2013

Keywords:

SOFC

Interconnect

Scale growth rate law

Chromium oxide

Degradation prediction

Dual atmospheres

ABSTRACT

The ohmic resistance caused by Cr₂O₃ scale formation on metallic interconnects (MICs) can significantly contribute to the overall degradation of SOFC stacks. For this reason oxide scale growth on Cr₅Fe₁Y₂O₃ (CFY) and Fe₂₂Cr_{0.5}Mn (Crofer) was investigated by scanning electron microscopy (SEM) from post-test samples that were either exposed to air at 850 °C (furnace) or operated in Hexis planar SOFC-stacks under dual atmospheres (anode and cathode conditions) at temperatures around 900 °C. The study includes unique test results from a stack operated for 40,000 h. To analyze inhomogeneity in scale thicknesses a dedicated statistical image analysis method has been applied. SEM images were used to compare the structural phenomena related to MIC oxidation at different sample locations. The observed differences between different sample locations may relate to locally different conditions (temperature, pO₂, H₂O/O₂-ratio). Cr₂O₃ scale growth on the anode side is found to be approximately twice as fast in comparison to the scale growth on cathode side. Finally, based on our time lapse analyses with extensive sampling it can be concluded that reliable predictions of scale growth requires statistical analyses over a period that covers at least a quarter (10,000 h) of the required SOFC stack lifetime (40,000 h).

© 2013 Elsevier B.V. All rights reserved.

1. Introduction

Solid oxide fuel cell (SOFC) based combined heat and power (CHP) systems are currently introduced to the market [1–4]. For commercially viable stationary CHP-systems a required stack lifetime of 40,000 h, with an average power degradation rate below 1% per 1000 h [5], are targeted. It is obvious that the used components and materials cannot be extensively tested and characterized for such a long period. The SOFC community needs reliable lifetime

predictions for SOFC stacks in order to minimize the development time and costs for this promising technology.

Recent improvements of the reduction–oxidation (redox) stability of SOFC fuel cells [2,6,7] caused a reinterpretation with respect to the weighting of the major degradation effects that are induced by high temperatures and oxidative atmospheres of SOFC operation, coming along with corrosion and microstructural changes. A major contribution to long-term degradation (>10,000 h) is brought by the oxidation of the metallic interconnects (MIC) [8]. Interconnects act as gas separators and distributors for cathode air and anode fuel as well as current collectors from these electrodes [9–12]. The ideal properties for materials

* Corresponding author. Tel.: +41 58 934 7717; fax: +41 58 934 7797.

E-mail addresses: MarkusLinder@gmx.ch, markus.linder@zhaw.ch (M. Linder).

used in interconnects are as follow: i) oxidation and corrosion resistance, ii) high electrical conductivity, iii) coefficient of thermal expansion (CTE) matching to cell components, iv) mechanical durability, v) low volatility of constituents, vi) chemical compatibility with adjacent materials and vii) low material and manufacturing cost [9,10,13].

Fe- and Cr-based alloys achieve a reasonable compromise in fulfilling these multifaceted properties requirements, including a CTE similar to ceramic cell components. Such alloys are chromium formers, i.e. a semi-conductive Cr_2O_3 scale is growing upon surface oxidation, which introduce a corrosion resistance at the contact between MIC and electrode [10,11,14]. Hence, the main problem with Cr_2O_3 scales is the formation of a layer with low electric conductivity compared to the base-alloy, which leads to unwanted ohmic losses. To reduce these losses and to predict their impact on the long-term power degradation it is necessary to understand the time dependent mechanism of scale formation under stack operating conditions.

A possible strategy to reduce the formation of an oxide layer is the additions of reactive elements (RE), which lead to a change of the scale growth mechanism [15,16]. It is assumed that outward diffusion of Cr along grain boundaries is hindered so that the slower oxygen inward diffusion becomes the dominant process in scale growth. Thereby, the oxide formation takes place at the interface between metal substrate and the oxide scale [16]. This improves scale adherence and reduces the oxidation rate [10,14–17]. In detail, the involved mechanisms yielding these improvements are however unclear [15]. The elemental mixed oxide dispersion strengthened (ODS) composition $\text{Cr}5\text{Fe}1\text{Y}_2\text{O}_3$ (CFY) (cf. Table 1) is an example of such a Cr_2O_3 scale forming material. It contains small amounts of Y_2O_3 as a reactive element. The CTE of this alloy is ca. $10.4 \times 10^{-6} \text{ K}^{-1}$ (around 900 °C) and fits well to electrolyte supported cells.

Crofer 22 APU ($\text{X}1\text{CrWNbTiLa}22$) and Crofer 22 H ($\text{X}1\text{CrWNbTiLa}22$) are other established SOFC MIC materials. Their compositions are given in Table 1. These Fe-based alloys combine surface oxidation stability with enhanced electrical conductivity for the oxide scale and a CTE matching to anode-supported cells. These alloys contain La as a reactive element. By the addition of Mn (≈ 0.5 wt.%) a $(\text{Mn,Cr})_3\text{O}_4$ spinel layer is formed on top of the Cr_2O_3 sub layer. The electrical conductivity of $(\text{Mn,Cr})_3\text{O}_4$ is five times higher at 900 °C than Cr_2O_3 [10,11,14,18–20]. Moreover, the Cr volatility of the $(\text{Mn,Cr})_3\text{O}_4$ spinel phase is roughly three times lower compared to spinel free Cr-oxide scales such as the ones formed upon oxidation on CFY [10,11].

In fuel cell stacks Cr_2O_3 scale exposure to water vapor containing atmospheres promotes the formation of volatile Cr species [13,18,21]. Under certain condition, this volatilization leads to chromium poisoning due to the accumulation of Cr within cathode layers [22,23]. For improved properties regarding Cr evaporation, surface modifications and coatings are usually applied on the MIC [9,10,24,25]. Effective coatings lead to an improvement of the

following properties: i) reduction of Cr diffusion from the metallic interconnect to the cathode, ii) chemically compatibility with adjacent SOFC materials, iii) high electric conductivity and iv) a CTE close to one of the MIC to avoid spallation [9,10,24,25].

The aim of this work is to quantify the oxide scale growth rates for metallic interconnects in stationary SOFC–CHP systems. This information is considered as a basis, which is then needed in a later stage (i.e. work in progress) to establish quantitative relationships between the oxide growth with the corresponding ohmic loss over the complete device lifetime. For the quantitative description of scale formation in the present study, a large amount of scanning electron microscopy (SEM) images is analyzed and quantified by applying a simple imaging processing method. Oxide dimensions are assessed from heat-treated MIC samples as well as from post-stack test samples. The latter are extracted from fuel cell stacks operated with pre-reformed (catalytic partial oxidation, CPOx) natural gas. This investigation also includes a unique set of post-endurance samples, obtained after completing and dissecting a CFY interconnect-based planar stack having reached 40,000 h of operation in a Galileo 1000 N system from Hexis [2]. The results are discussed also in comparison with the relevant literature data. It must be emphasized that a systematic correlation of oxide growth with ohmic losses is part of ongoing research, which will be addressed in a separate paper.

2. Experimental details

Scale growth rates are determined by oxide size measurement from samples out of interconnects after stack-testing and from samples heat-treated in a furnace. During the heat treatment tests only cathode conditions are simulated. From the stack test samples, the oxide formation can be investigated for both atmospheres, cathode as well as for anode conditions which is called “dual atmosphere” test. The assessment of growth kinetics is based on time-lapse microscopy, i.e. scale dimensions are quantified with scanning electron microscopy (SEM) and image analysis for different time steps.

The investigated interconnects have a fluted structure in order to provide the fuel to the anode and the air to the cathode, respectively. Thereby the ridge tops are basically used as contacts with the electrode in order to ensure the electron transport within a stack(ed) configuration between the repeat units (RUs). Throughout this manuscript this top region is denoted as flat whereas the bottom of the gas channels is denoted as valley. This specific terminology for the fluted interconnect structure is also illustrated in the schematic cross section in Fig. 1.

2.1. Layer thickness determination

The layer dimensions of Cr_2O_3 scales are determined on the basis of SEM image analysis of sample cross-sections. Therefore samples are cold mounted in epoxy resin and after hardening

Table 1

Composition of investigated materials (in wt.%) [57–60]. CFY is used in stack and exposure experiments. Crofer is used in exposure tests only. JS-3 composition is needed for comparison within the discussion section.

	Cr	Fe	C	N	Mn	Si	Cu	Al	W	S	P	Ti	Reactive elements	
													La	Y_2O_3
Crofer 22 APU	20–24	Bal. ^a	0.03 ^b		0.3–0.8	0.5 ^b	0.5 ^b	0.5 ^b		0.02 ^b	0.05 ^b	0.03–0.2	0.04–0.2	
Crofer 22 H	20–24	Bal. ^a	0.03 ^b	0.03 ^b	0.3–0.8	0.1–0.6	0.5 ^b	0.1 ^b	1–3	0.006 ^b	0.05 ^b	0.02–0.2	0.04–0.2	
JS-3 ^c	23.3	Bal. ^a			0.4	0.009		0.005				0.047	0.089	
CFY	Bal. ^a	5												1

^a Difference to 100 wt.%.

^b Maximum amount.

^c Semi-commercial Crofer 22 APU [55,60].

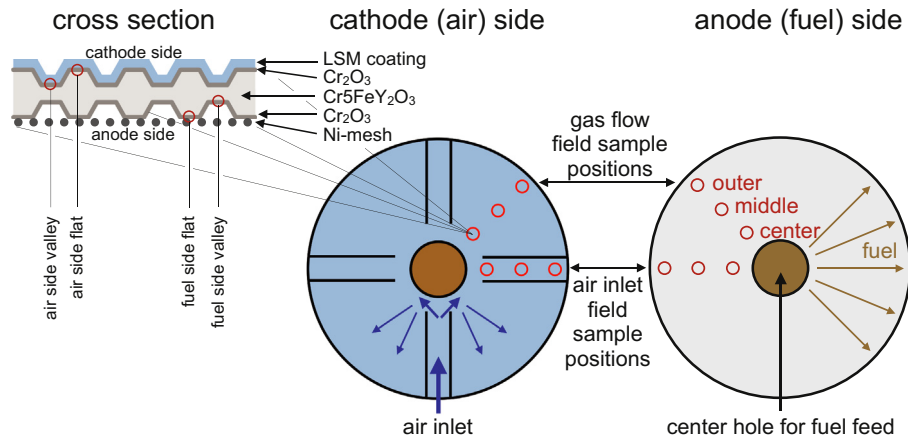


Fig. 1. Schematic illustration of Hexis' MIC design. The blue disk in the middle pictures the flow path on the cathode side. Each quadrant comprises an inlet channel, with air fed from the outer edge. The flow direction is deviated near the central hole to reach a co-flow regime within the main area of the cell. The right side illustrates the anode flow field where the fuel flows from the central hole (co-flow) to the outer edge. The red circles mark the locations of sample extraction. As shown on the left side, anode, cathode as well as flat and valley are analyzed for all six sample locations. (For interpretation of the references to color in this figure legend, the reader is referred to the web version of this article.)

grinded and polished with SiC papers up to 4000 grit on a Struers TegraPol-35. SEM images are taken on a Tescan VEGA TS 5130 MM with the backscattering detector. This microscope is equipped with an INCAx-sight from Oxford Instruments for energy dispersive X-ray spectroscopy (EDX). To generate representative results up to ten SEM images are analyzed for each sample location as given in Fig. 1, e.g. the contacting flat on the anode side. The number of images that is necessary for a representative analysis varies as a function of sample location and magnification of an investigated area. For thicker layers, found at longer exposure time, the magnification can be reduced and hence a smaller number of images is required. The quantification process is illustrated in Fig. 2. Therefore the Cr_2O_3 layer is identified based on its gray-scale contrast. After segmentation with the Adobe Photoshop CS5 image processing software the (black) pixels representing the Cr_2O_3 layer are counted. For each image, the mean layer thickness is then calculated by dividing the number of black pixel with the image width. This result is then multiplied by the corresponding pixel size. Counting and calculation steps are done automated with the computational tool Mathematica 8.0. Note: image orientation is always perpendicular to the MIC surface.

2.2. Heat treatment tests

In these heat treatment tests, four different materials are investigated; these are Crofer 22 APU, Crofer 22 H, CFY and LSM coated CFY. Their elemental compositions are given in Table 1. All compounds present a fluted-structure (Fig. 1) that is comparable to a MIC and ensures fuel and air distribution (valley) as well as current collection (flat) in a stack(ed) configuration. The samples are exposed to 850 °C at ambient air in a Carbolite CWF 12/13 box furnace without an additional air circulation. Heating rate is 3 °C min⁻¹. For the different time steps up to 5,300 h the furnace was cooled down to remove probes at each time step for time lapse microscopy.

2.3. Observation of surface crystal formation on a heat-treated sample

A specific surface location on an uncoated CFY sample was marked in order to follow the growth of individual surface crystals at different time steps. The marked sample was exposed together

with the heat treatment samples at the same time and under the same conditions. This sample was always removed from the box furnace during ordinary samples removal for the time lapse microscopy. Before the furnace at any one time was reheated the

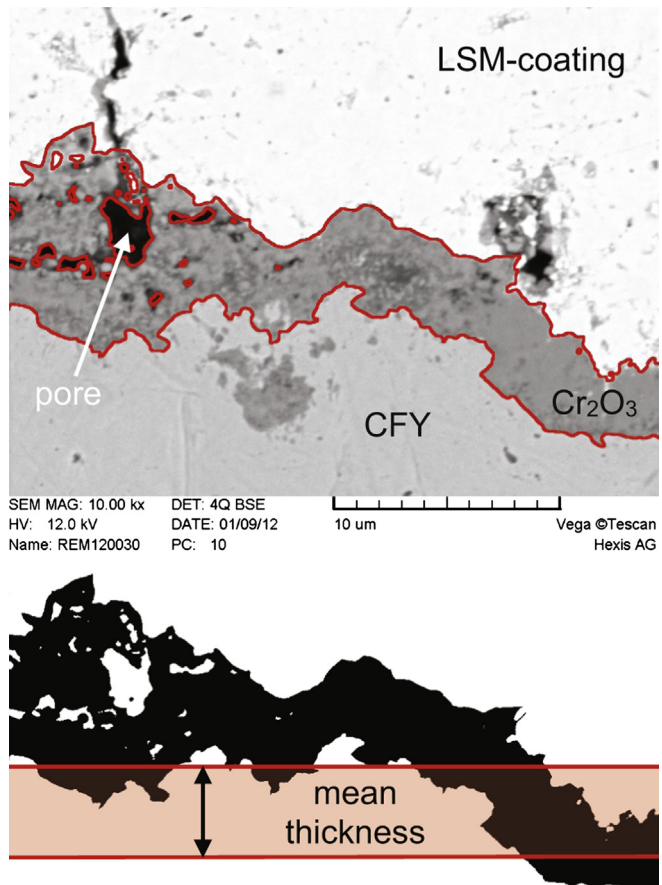


Fig. 2. (Top) SEM image of a cross section of a metallic interconnect after 2000 h exposure (850 °C in air). The perimeter of the Cr_2O_3 scale is marked by a red contour line. (Bottom) From the segmented and binarized SEM image a mean scale thickness is calculated. (For interpretation of the references to color in this figure legend, the reader is referred to the web version of this article.)

surface of this specific sample was investigated on the marked location by SEM analysis with the secondary electron detector.

2.4. Post-test stack samples

Oxide scale growth on the CFY MIC from SOFC stacks was assessed by analyzing more than 1000 SEM images from 30 samples, which were extracted from different CFY interconnects that had been operated for several thousand hours in five different stacks at 900 °C. These on the cathode side with LSM coated MICs were operated under dual atmospheres SOFC conditions. This implied the simultaneous exposure to anode fuel and cathode air environments. Testing conditions involve ambient air and pre-reformed (CPOx) natural gas (NG) from the local grid at Winterthur (Switzerland). The reformat mainly consists of N₂, H₂, CO, CH₄ and a certain amount of H₂O depending on the fuel utilization and the current load. Variations in the natural gas composition are ineluctable in the natural gas grid [26], especially within 40,000 h operation. Such long-term testing also inevitably involves incident as well as maintenance shut downs, leading to thermo and full redox cycles which means that the whole anode is oxidized in the sealing-less stack design. Detailed operating conditions are given in Table 2.

In this work, the samples from the Galileo stack were removed from the middle part. Despite of the convex temperature profile along the vertical direction it can be assumed that the samples from both short- and system stacks have experienced the same temperatures of 900 °C (Table 2).

Within a repeat unit the scale growth rates may vary. This is due to local variation of parameters such as temperature gradients, oxygen partial pressure (pO₂), water partial pressure (pH₂O) or gas flow rates. In order to quantify those variations six samples are taken from different locations of each single MIC. The positioning of the sample extraction locations within the MIC flow-field is given in Fig. 1.

3. Results

3.1. Layer thickness determination

The size distribution for the analyzed amount of SEM images at each single sample location is investigated to ensure that the applied oxide scale size quantification gives a representative mean scale thickness. Such a distribution is shown in Fig. 3. The distribution in this example based on the data out of nine SEM images (flats) over each single pixel column follows a normal distribution. A similar behavior is usually observed for all sample locations. This confirms that the applied method is reliable to determine a mean oxide scale thickness based on the analyzed SEM images.

Table 2

Operating conditions and test history of investigated stacks. Cell and MIC area in this round planar stack is 100 cm², respectively.

Operating hours	Stack type	Fuel	Reformat	No. of redox	MIC temp.	Fuel flux ^a	Air flux ^a	Load ^b	Cell contact	
									Fuel side	Air side
4200 h	Short	NG	CPOx	2	900 °C	4 g h ⁻¹	200 g h ⁻¹	25 A	Ni-mesh	LSM ^c
5700 h	Short	NG	CPOx	0	900 °C	4 g h ⁻¹	200 g h ⁻¹	25 A	Ni-mesh	LSM ^c
10,700 h	Short	NG	CPOx	2	900 °C	4 g h ⁻¹	200 g h ⁻¹	25 A	Ni-mesh	LSM ^c
13,200 h	Short	NG	CPOx	24 ^d	900 °C	4 g h ⁻¹	200 g h ⁻¹	25 A	Ni-mesh	LSM ^c
40,000 h	Galileo	NG	CPOx	15	900 °C	4 g h ⁻¹	— ^e	0.72 V	Ni-mesh	LSM ^c

^a For a single RU.

^b Either constant current or constant voltage.

^c LSM coating on cathode side.

^d 20 redox cycles within the first 800 h.

^e Air flux is varying with discharged heat amount to keep the stack temperature constant (temperature controlled).

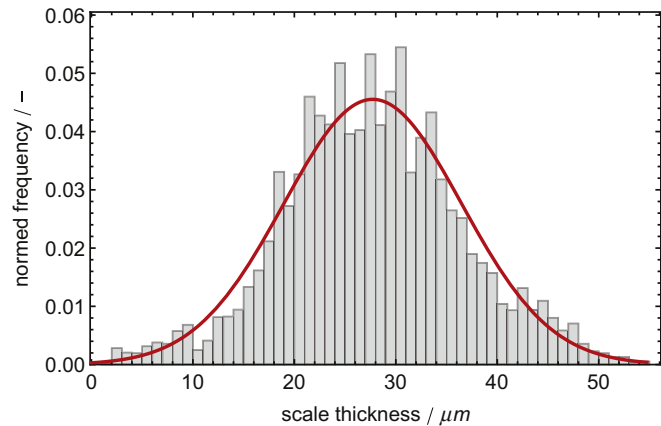


Fig. 3. Scale size distribution based on single pixel columns out of nine SEM images from a sample located in air inlet channel in the middle region on flat at anode side after 5700 h stack operation (cf. Fig. 1).

3.2. CFY interconnect oxidation under dual atmospheres exposure in stacks

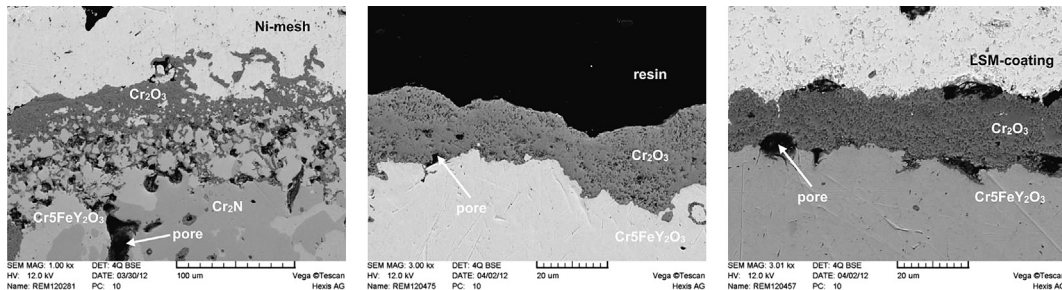
In the following section we first present a qualitative description of the main microstructural features associated with scale growth and then we discuss the local quantitative variations on the anode and cathode sides.

3.2.1. Qualitative variations in the microstructure

An illustration of the main microstructural features is shown with three representative images in Fig. 4a–c. On Fig. 4a (anode side) interaction of the Cr₂O₃ scale with the Ni-mesh leads to the formation of a patchy layer, which contains metallic Ni-grains (bright) that are embedded in a Cr-oxide matrix (gray). This scale-structure is typical for the flat on the anode side (center position). Below this outer Cr-oxide layer the upper part of the MIC is transformed into a porous zone, which contains metallic grains (from the initial MIC) as well as oxides (Cr₂O₃ mainly). This layer is subsequently called “internal oxidation layer”, because the oxidation is growing inwards from the initial MIC surface. Underneath the porous, internal oxidation layer an additional phase (darker than CFY, but brighter than Cr₂O₃) is observed on SEM/BSE images. This phase is identified as Cr₂N by EDX spot analysis and it is a typical feature for the center position on the anode side.

Fig. 4b shows the valley at the outer position of the anode side. The scale is composed of a homogeneous Cr₂O₃ layer marbled with pores. In contrast to the center position, there is no internal oxidation layer and no formation of Cr₂N at the outer position.

Fig. 4c is representative for the scale structure on the cathode side. A relatively homogeneous Cr₂O₃-layer is formed between MIC



(a) Anode side, center position, flat location: strong internal oxidation, few pores within the Cr_2O_3 scale, nitride formation beneath the oxide layer and some Ni-mesh interaction.

(b) Anode side, outer position, valley location: pores are present within the oxide scale.

(c) Cathode side, middle position, flat location: pores are formed at the scale interfaces.

Fig. 4. Scale characteristics for cathode/anode | flat/valley locations after 10,700 h short-stack operation with CPOx reformed natural gas. These SEM backscattered electron images illustrate the trends for the Cr-oxide microstructures given in Table 3. NB: magnifications differ for sub-figures (a), (b) and (c).

(bottom) and LSM layer (top). The layer contains pores whereas some of them are formed at the interfaces to the MIC and to the LSM protection layer. Furthermore the formation of $(\text{Cr},\text{Mn})_3\text{O}_4$ spinel was identified with SEM and EDX (see Fig. 12 and corresponding discussion in Section 4.3), which appears to be typical for the oxidation of cathode MICs with an LSM protection layer (not shown in Fig. 4).

Based on the described observations four main structural features associated with MIC scale growth can be observed. These features, which may vary as a function of the sample location, are the following: i) the internal oxidation layer (anode side), ii) the formation of pores within the oxide layer and at its interfaces with the adjacent MIC or LSM layers, iii) the formation of Cr_2N in the MIC and iv) interactions between Cr-oxidation layer with the adjacent current collector materials (i.e. Ni-mesh on anode side, LSM on cathode side).

Based on the extensive sampling for all 12 sample locations as described in Fig. 1 (i.e. air inlet and gas flow fields | center, middle and outer positions | flat and valley) a systematic pattern of microstructural variations can now be characterized. These variations are summarized qualitatively in Table 3 and they can be described as follows:

First of all it is important to note that the scale structures on the cathode side are more homogeneous than on the anode side. On the cathode side differences are neither observed between flat and

valley nor between the air inlet and gas flow fields. Hence, for all sample locations on the cathode side the structures are similar as shown in Fig. 4c.

On the anode side the scale characteristics are changing as a function of the sample location. The formation of an internal oxidation layer (with pores) is typically observed at the center and middle positions. In the outer positions this layer is weak on the flats and it is completely missing on the valleys. The formation of pores is a characteristic feature at the valley of the outer positions. In contrast Cr_2N is only observed in center and middle positions. There are thus clear differences on the anode side between different radial positions (center, middle, outer) and between flat and valley. However there are no structural differences between equivalent positions in the air inlet and in the gas flow fields.

3.2.2. Quantitative variations in the scale thickness

In this section we are focusing on the quantitative description of the mean scale thickness (and its evolution over time), by using the procedure illustrated in Fig. 2. A representative example for the extent of MIC oxidation at different sample locations and after a given operating time is shown in Fig. 5. This result comes from a five cell short stack that had been operated for 10,700 h at 900 °C with CPOx reformed natural gas. Mean scale thicknesses are presented for the different sampling locations. Each data point is obtained from numerous SEM images. The mean (red diamond) and

Table 3
Trends of oxide scale characteristics for all 24 sampling locations (Fig. 1) assessed for 5 stacks with 1000 SEM images. The specific characteristics are exemplary given in Fig. 4.

		Air inlet field						Gas flow field					
		Flat			Valley			Flat			Valley		
		Center	Middle	Outer	Center	Middle	Outer	Center	Middle	Outer	Center	Middle	Outer
Anode	Internal oxide	●	●	○	●	●	○	●	●	○	●	●	○
	Pores only within the oxide scale	○	○	○	○	●	●	○	○	○	○	●	●
	Cr_2N	●	●	○	●	●	○	●	●	○	●	●	○
	Ni-mesh interaction	●	○	○	○	●	○	●	○	○	●	●	○
Cathode	Internal oxide	○	○	○	○	○	○	○	○	○	○	○	○
	Pores within the oxide scale and at the interfaces	●	●	●	●	●	●	●	●	●	●	●	●
	Cr_2N	○	○	○	○	○	○	○	○	○	○	○	○
	LSM interaction as CrMn_2O_4 -spinel formation	●	●	●	●	●	●	●	●	●	●	●	●

○ Not observed.

● Partly observed.

● Observed.

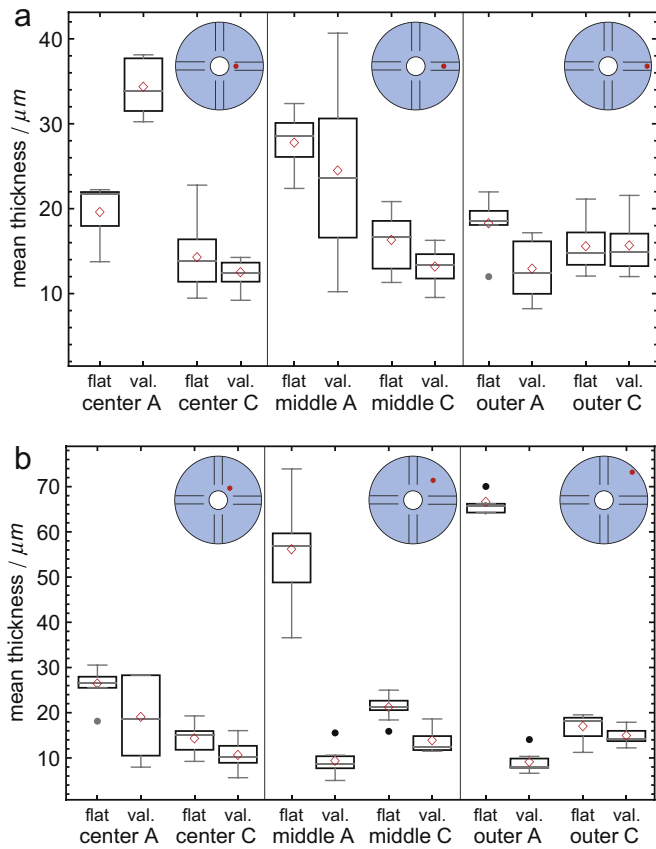


Fig. 5. Box-whisker charts for the distributions of the mean scale thickness after 10,700 h operation. These samples were extracted at different locations (given in Fig. 1) in the air inlet channel (upper diagram a) and the gas distribution field (lower diagram b). The denominations center, middle and outer specifies the different radial positions. A and C stand for the anode side and the cathode side, respectively.

median (gray line) thicknesses as well as the upper and lower quartiles present some scatter of the data in this box-whisker chart. Quantitative trends are however clearly identified with such a statistical representation. The anode scale thickness is higher than on the cathode side, i.e. scale growth rates are higher in the fuel compartment with lower oxygen partial pressure and presence of steam. Anode flat oxide layers are thicker than at valley locations where no covering with a Ni current-collecting material is present. The latter trend, higher oxide amounts on the flat compared to the valley, is also observed on the cathode side, although less pronounced. For both cathode and anode side, no systematic quantitative differences are evidenced between the various sample locations, neither for sampling within the air inlet region nor within the gas flow fields with respect to radial shifts. However, as shown in Table 3, there are some qualitative microstructural features that vary with sample locations.

Systematic quantitative differences are only found between anode and cathode as well as between flat and valley and not for the different sampling locations. All scale thickness measurements within a MIC are averaged for the following four categories: anode flat, anode valley, cathode flat and cathode valley. These results are plotted in Figs. 6 and 7 for different stack tests.

3.3. Oxide scale growth rates during stack operation

In order to describe the scale growth rate the data from time laps microscopy was first fitted with a parabolic rate law that is based on Wagner's oxidation theory according to Eq. (1):

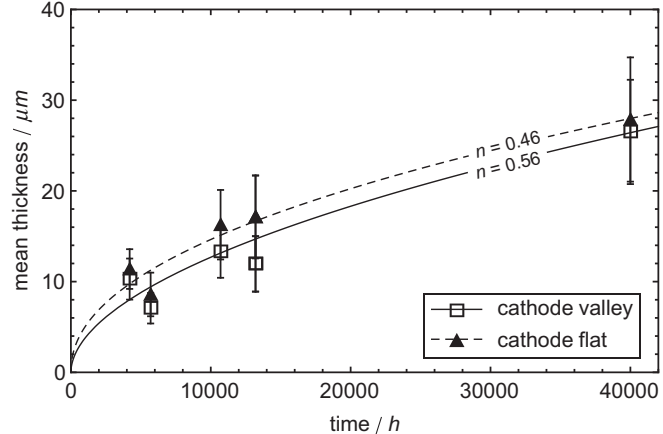


Fig. 6. Cathode side MIC oxidation evolution in stacks. Flat scales (closed symbols) are systematically thicker than valley oxide layers (open symbols); the difference is however small. The mean data points follow a parabolic growth law, where the exponents fitted by Eq. (2) are close to $n = 0.5$.

$$x^2 = k_p t \quad (1)$$

where x is the mean scale thickness, t the operating time and k_p the parabolic rate constant. However, in most cases the parabolic rate law is unsuitable to describe chromium oxide scale growth rates especially at longer exposure time. Therefore the data was fitted with a more generic exponential relation:

$$x = k_e t^n \quad (2)$$

where k_e is the exponential rate constant and n the exponent. This relation better describes the often reduced growth rates at exposure times longer than several hundred hours. Such reduced growth rates are observed for alloys that contain reactive elements (RE) [27]. Thereby the reactive elements prevent outward diffusion of metal ions e.g. Cr^{3+} [16].

As shown in Fig. 6 the growth rate exponents for the cathode side are close to $n = 0.5$. The scale growth on the cathode side can

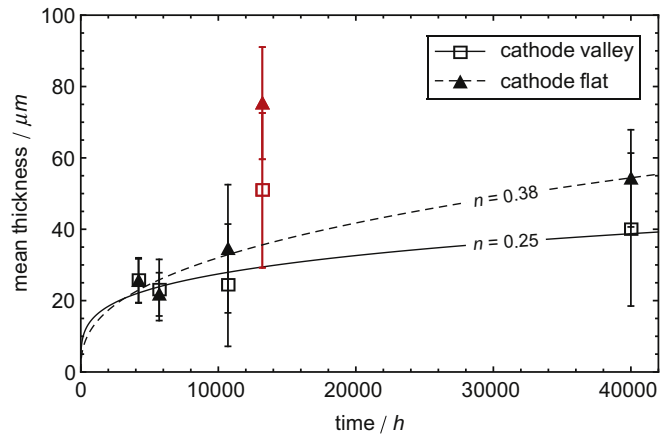


Fig. 7. Oxide scale growth on the anode MIC upon stack testing up to 40,000 h. Open symbols represent mean values of calculated scale thicknesses for flat regions. Closed symbols represent mean values from valley cross sections. The curves are based on data fits with Eq. (2) without considering the data points at 13,200 h (red marked). These samples are derived from a stack with 20 redox cycles within the first 800 h of operation. The exponents ($n = 0.38$ for flat, $n = 0.25$ for valley) indicate a non-parabolic scale growth on the anode side. (For interpretation of the references to color in this figure legend, the reader is referred to the web version of this article.)

thus be interpreted as being parabolic. In contrast the exponents describing oxidation on the anode side (Fig. 7) are clearly smaller (i.e. $n = 0.25$ for anode valleys and $n = 0.38$ for anode flats). However for the fits the data points at 13,200 h (red marked) are not considered on the anode side. This data are derived from five cell short stack which was operated with 20 full redox cycles during the first 800 h of operation. As a result of this operation mode the oxide scale on anode side is significantly enlarged and does obviously not match to the overall scale size development. In contrast some influence by these redox cycles during initial stage to the quantitative oxide scale formation on the cathode side is not indicated (Fig. 6).

When comparing absolute scale thicknesses in Fig. 6 (cathode side) and 7 (anode side) with each other it becomes apparent that the oxide layers on the anode side are thicker despite of the smaller n -values. This is attributed to a higher exponential rate constant k_e , which leads to formation of relatively thick oxide layers on the anode side during the first few hundred hours. Furthermore it is important to note that the scales on the flat are systematically thicker than on the valley. These local differences are also observed on the cathode side. However, there they are less pronounced.

3.4. Scale thickness and growth rates derived from heat treatment tests

To investigate and compare some effects of different materials and to interpret the results from stacks tests, MIC samples of four different materials were additionally exposed in ambient air up to 5'300 h. The results of such model experiments are more comparable to literature data, which are usually collected in a similar way. Fig. 8 shows the time dependence of the mean oxide layer thicknesses (values are calculated from over 300 SEM images) for CFY, CFY coated with LSM, Crofer 22 APU and Crofer 22 H. The growth characteristics during the first 500 h are similar for all four materials. At longer exposure time (i.e. ≥ 2000 h) oxide thicknesses for Fe-based alloys are larger than for the Cr-based CFY. Hence different growth rates and exponents are determined for the two material types by fitting the data with Eq. (2). The exponent obtained for the Crofer 22 APU is equivalent to $n = 0.5$. Also Crofer 22 H with $n = 0.46$ follows an oxidation behavior close to a parabolic rate law. For the LSM coated and uncoated CFY the exponents are $n = 0.36$ and $n = 0.39$, respectively. In this context it should be emphasized, that the experiment in Fig. 8 is performed under static conditions (i.e. no airflow). As shown by Stanislowski et al. [21] in the static

case equilibrium is reached between evaporation and reprecipitation (called “equilibrium vaporization”) and thus, no significant influence of evaporation on the growth rate is expected. This may explain the similar scale growth rate and behavior of coated and uncoated samples.

3.5. Surface oxide formation on a heat-treated sample

To investigate the surface oxide formation on the RE containing CFY a discrete spot was analyzed for the different time steps. Fig. 9 show the development of surface crystals during heat exposure. The final arrangement and shapes of surface crystals are recognizable already after 10 h heat exposure. A tendency for covering the original crystals by the formation of new crystal nucleus could not be observed which means that further oxide scale growth takes place at the scale/alloy interface or somewhere within oxide scale. The quantitative assessment of surface crystal growth is given in Fig. 10, which points out that the initially high growth rates reduce to moderate rates after 100 h. After 2000 h, the surface crystal growth is terminated and no significant surface alterations are visible at longer exposure times.

4. Discussion

The comparison between Figs. 6 and 7 shows that the oxide growth rates for 40,000 h stack operation deviate from Wagner's oxidation theory. Thereby oxidation progresses faster on the anode side of the SOFC MICs. Bringing these results together with literature data should strengthen our findings. Direct comparison with growth rates from other research groups is however difficult as different test conditions, sample preparation methods and geometries as well as assessment methods are involved [27–30]. The oxidation is generally estimated from weight gain measurements and sometimes correlated to scale evolution in post-test observations [30]. Even for similar test conditions, scale growth rate predictions in literature tend to be smaller up to a factor of five [30]. We deduce that the limited time-spans over which the oxidation behavior is generally assessed, lead to a high uncertainty of results. Such investigations generally cover insufficient exposure times, typically below 500 h [19,31]. From Fig. 8 it becomes apparent that the data points related to short exposure times (i.e. <1000 h) show a significant divergency instead of defining clear trend lines. This scattered picture becomes even more evident when the n -values are determined for each single data point while keeping the rate constant k_e fixed. The corresponding results are shown in Fig. 11. Again, the n -values obtained for short exposure times show a large variation, whereas at exposure times >500 h the obtained n -values are uniform. A possible explanation for this scatter may be related to the fact that the scale growth at short oxidation times is dominated by local heterogeneities (such as presence and absence of pores or variable concentrations of reactive elements etc.) and different mechanism. In any case, the results document that the growth rates relevant for long-term prediction cannot be derived from experiments that cover only the initial oxidation period. Obviously, only after approximately 500 h (or even more) a steady state oxidation regime relevant for long-term operation is reached.

4.1. Scale growth rate description

Different mathematical functions, which deviate from Wagner's theory (Eq. (1)) describe the scale growth for various materials and oxidation stages. A logarithmic rate law addresses metal oxidation at low temperatures (below 300–400 °C). Under such conditions the initially fast scale growth reaches a negligible rate due to the formation of a blocking oxide layer. In contrast, the linear rate law

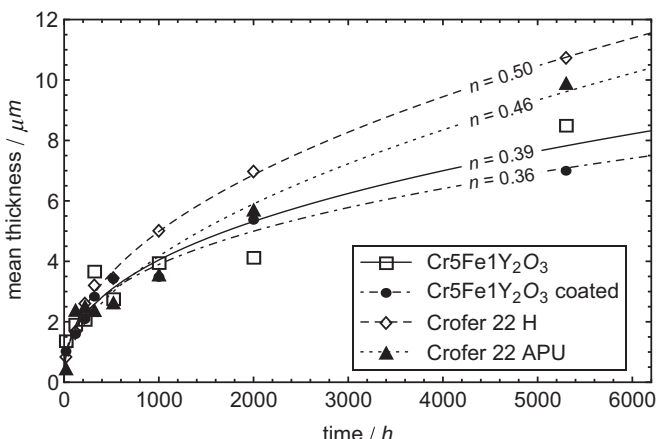


Fig. 8. Oxide scale growth derived from exposure tests (850 °C in air) for different MIC materials. The lines show the fitted growth rates according to Eq. (2). The variation of exponent n indicates different oxidation mechanism for such material configurations.

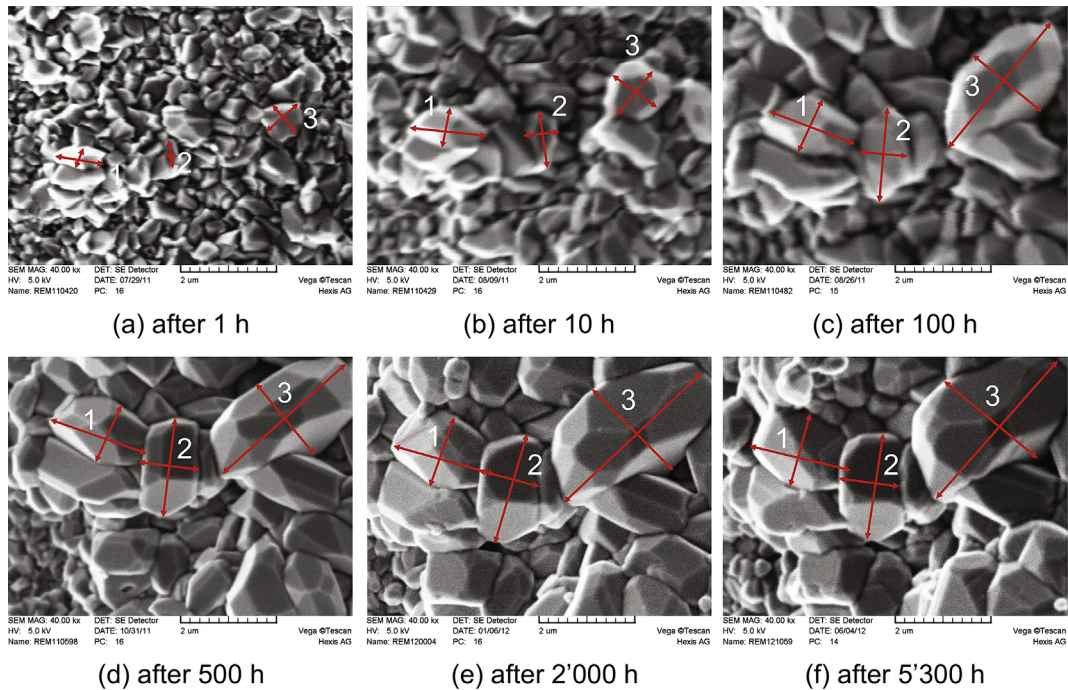


Fig. 9. This series of SEM images shows the qualitative chronology of crystal development on a CFY surface exposed to air at 850 °C. All images are taken from the same sample location, which is marked, to ensure that always the same spot is considered. The red arrows are used to quantify the crystal growth rates (reported in Fig. 10).

describes scale growth mechanisms taking place in priority at the outer scale surface. Such a linear reaction rate is independent of the consumed amount of metal or gas, which is e.g. characteristic for the initial oxidation period. The different reaction rates combine upon occurrence of diverse oxidation stages during long-term oxidation [16]; the resulting oxidation law deviates from a parabolic description [27,32,33]. It is also pointed out by Quadakkers et al. [11] that the description of the complex scale growth mechanism based on experimental data can only by accident be described by a parabolic rate law. A combined rate law is suggested by Kofstad [16] and corresponds to Eq. (2). The superimposition of changing oxidation stages with time induces a time dependence of the exponent n and the grow rate constant k_e . Fig. 11 therefore shows the exponent n that is determined for each data point with a fixed rate constant k_e . The resulting time evolution of exponent n

illustrates data scattering for the first 500 h induced by the adjustable growth states in the initial oxidation phase.

A similar behavior was observed by monitoring the surface crystal growth on CFY (Figs. 9 and 10). The fast surface crystal formation during the first few hours of heat treatment is decelerating gradually. This observable process is widely finished after 500 h heat exposure. This observation, together with the enlarged scattering of the exponent n (Fig. 11), indicates the oxide scale growth during the first few hundred hours (<500 h) to be governed by different overlaying mechanisms. Therefore we deduce that the experimental characterization of oxidation after long-term exposure (>10,000 h) is needed to ascertain a reliable quantitative description of the growth behavior, which takes into account the oxidation mechanisms relevant for SOFC device lifetime predictions.

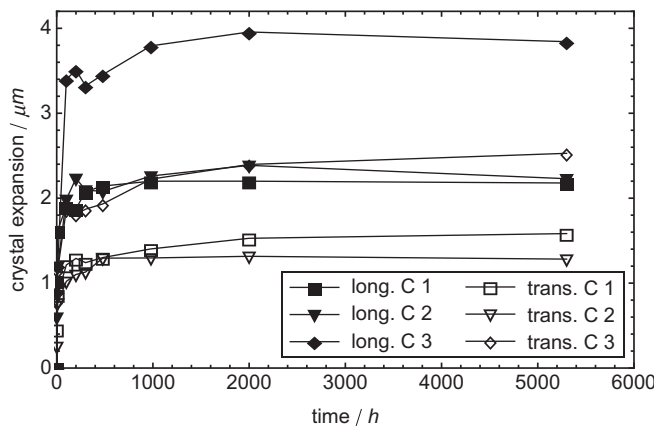


Fig. 10. Longitudinal and transversal growth rates for single crystals based on the surface observation presented in Fig. 9. This CFY sample was exposed to air at 850 °C. C1, C2 and C3 are individual oxide crystals.

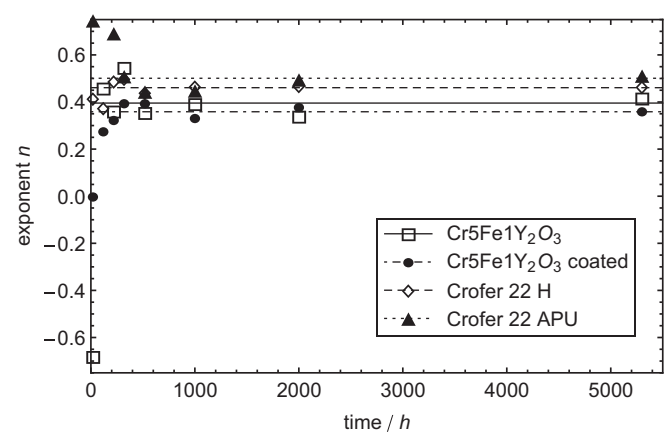


Fig. 11. Exponents n according to Eq. (2) for fixed rate constants k_e show a large scatter within the first 500 h.

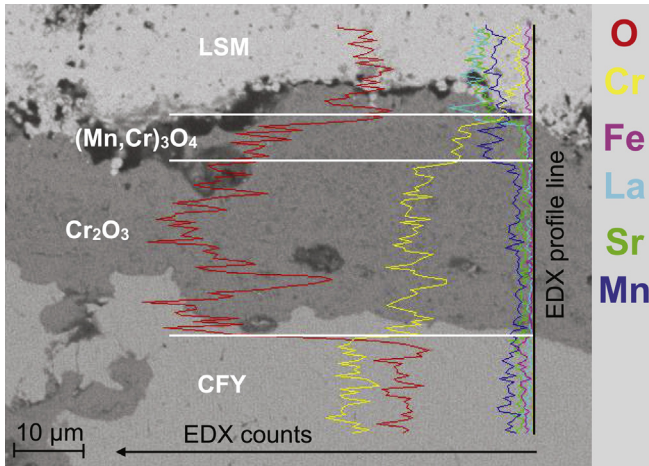


Fig. 12. SEM/BSE image with EDX line scan of LSM coated CFY after 40,000 h stack operation. A weak BSE contrast reveals the formation of a distinct $(\text{Mn},\text{Cr})_3\text{O}_4$ spinel-layer at the LSM/ Cr_2O_3 interface, which is confirmed by the EDX line profile. EDX spot analysis for the spinel phase reveals the following compositions: Cr = 23.6 at.%, Mn = 13.4 at.%, O = 63.0 at.%

4.2. Scale growth influencing parameters

Both quantitative and qualitative oxidation characteristics are influenced by various SOFC design- and operating-dependent parameters, such as MIC composition (alloying elements), temperature and steam contents (both dependent on fuel utilization) as well as adjacent components (coating and contacting materials).

Oxide scale growth rate is strongly affected by the temperature. With increasing temperature the growth rate constant increases exponentially [16,30,34,35]. The box-whisker charts (Fig. 5 represent only one example) show no systematic trends for the mean scale thickness in correlation with the sample positioning (i.e. air inlet and gas flow fields | center, middle and outer positions) on the MIC. This corroborates the influence of the high heat conductivity of CFY, which leads to a homogeneous temperature distribution on the MIC. The scale thickness on flat is however enlarged in comparison to the valley. This may be caused by a minimal local temperature rise due to the ohmic losses under locally high electrical current densities.

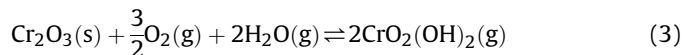
The oxygen partial pressure is also known to influence the oxidation rate. Increasing Cr_2O_3 growth is reported for reduced O_2 partial pressures down to a certain limit [29,36] which is in general compatible with our observation of thicker scales on the anode side. Only a minor pO_2 reduction is observed on the cathode side, due to O_2 consumption under load. This is in agreement with constant scale thickness distributions over a cathodic MIC surface, which is also reported in literature [34,37]. Certainly we observed for the anode side a different behavior for the specific operation mode with extensive full redox cycling during the initial stage. The data points at 13,200 h in Fig. 7 (red marked) do not suit to the overall trend. Obviously the scale formation on anode side was accelerated by the alternating atmospheres during this 20 full redox cycles within the first 800 h. Such an influence on oxide scale formation related to redox cycles is mentioned by Bastidas [38].

The oxygen partial pressure that is influenced by the presence of steam plays a key role on the anodic MIC oxidation; in particular the $\text{H}_2\text{O}/\text{O}_2$ ratio is a relevant factor. The scale growth is enhanced with increasing $\text{H}_2\text{O}/\text{O}_2$ ratios [29,39,40]. The Cr_2O_3 scale thickness on the anode side (Fig. 7) is clearly enlarged after 40,000 h in comparison to the cathode side (Fig. 6) that is exposed to a dry environment with a high O_2 partial pressure ($\text{pO}_2 > 10^4 \text{ Pa}$).

Thermodynamic calculations for the Hexis system have shown the pO_2 at nominal operating point under CPOx reformed natural gas to be below 10^{-14} Pa for the entire anode side. An increase up to 30% of the steam concentration is brought by fuel utilization along the radial position within a repeat unit, i.e. dry conditions near the center and humid atmospheres at outer cell regions. It must be emphasized that the influence of the $\text{H}_2\text{O}/\text{O}_2$ ratio on Cr_2O_3 growth is still debated in literature [29]. But it is also reported that H_2O content along the fuel flow path positively influence the scale tightness and adhesion [11,13,29,41].

This suggestion is strengthened by the observation of a Cr_2N phase, which is present in the central region of anodic MICs (dark gray spots in Fig. 4a). Obviously the permeable oxide scales enable N_2 access ($\text{pN}_2 \approx 0.4$ in CPOx gas mixtures) to the CFY alloy. Nitrogen transport is suggested to occur preferably via gas transport rather than by solid state diffusion [11]. Hence gas diffusion occurs through oxide scales with insufficient tightness. Again, the gas tightness is improved in the outer region due to the increased water content. On the cathode side (Fig. 4c) Cr_2N formation is not observed, although the nitrogen partial pressure is two times higher in air than in CPOx reformed anode gas. The LSM coating and the Cr_2O_3 layer thus seem to act as a diffusion barrier for the N_2 .

Cr_2O_3 scale growth is also affected by evaporation of volatile Cr-species, in particular of $\text{CrO}_2(\text{OH})_2(\text{g})$ which is formed in humid atmospheres [21,42], according to the following reaction:



Chromium evaporation during stack operation occurs from the uncoated anodic MIC surface and also through cracks in the LSM coating on the cathode side. The anodic flat is capped with a nickel mesh, acting as a flow barrier, which reduces local flow rates and hence reduces Cr evaporation [21]. Fig. 7 indicates thinner oxide scales in valley locations that are exposed to the fuel/exhaust flow, which may trigger the evaporation. In contrast, on the cathode side no significant difference is observed between valley and flat (Fig. 6). This observation indicates that the airflow is suggested to only have a minor influence on Cr evaporation from the cathodic Cr_2O_3 scale, because it is fully covered with LSM.

Besides its Cr retaining property that consequently reduce cathode poisoning, the LSM interacts with the Cr_2O_3 scale to build a $(\text{Mn},\text{Cr})_3\text{O}_4$ -spinel layer at their interface [43]. This effect is confirmed for different samples by EDX analysis and is illustrated in Fig. 12. The $(\text{Mn},\text{Cr})_3\text{O}_4$ -spinel phase positively influences the electric resistance of the phase (by a higher conductivity) and furthermore reduces Cr evaporation [11,44,45]. On the one hand, literature data suggests LSM coatings to reduce MIC oxidation [28,46], on the other hand our results from the 5300 h exposure experiment does not clearly conclude on mitigated Cr_2O_3 growth (Fig. 8). Although the absence of Cr_2N indicates that LSM coatings exhibit gas tightness, the coatings do not prevent from oxygen diffusion that governs MIC oxidation [47].

Solid state hydrogen transport from the anode side to the cathode side can also influence the oxide scale formation under dual atmosphere operating conditions [35,48–50]. Such a solid state H_2 diffusion through Fe-based alloys is indicated by the formation of Fe oxide-rich nodules on cathode side on uncoated samples [35,48,50]. This dual atmosphere effect is decreased for alloys with increased Cr-content [49,51] as well as for increased sample thickness [35]. Also the formation of a dense oxide scale can lead to a significant reduction of hydrogen permeability [52]. In our investigations the ODS interconnect material has a relatively porous structure compared to Fe-based alloys. Therefore hydrogen transport through the interconnect material cannot be excluded. However, the formation of Fe-rich nodules could not be observed

on the investigated LSM coated CFY samples. These samples were operated under dual atmosphere in the SOFC stacks, but the stack experiments were not explicitly designed to detect solid state hydrogen transport and effects thereof.

The native lattice defect concentration in slow growing oxides, like Cr_2O_3 , is small [53]. Oxygen diffusion is therefore believed to essentially occur along the grain boundaries and is strongly influenced by the presence of impurities. The effect of differences in impurity levels on oxidation is given by Refs. [11,54] by comparing the high purity JS-3 to Crofer 22 APU (differences in composition are highlighted in Table 1). Such influence also explains the higher scale growth rates for Fe-based MIC with higher alloying amounts compared to the Cr-based CFY that only contains Y_2O_3 as RE. The sequences of scale growth rates derived after 5300 h of exposure (Fig. 8) are therefore compatible with literature data [11,30,54,55].

4.3. Scale growth dependent SOFC lifetime prediction

The major goal of this work is to give reliable quantitative predictions of the oxide scale development over the prospective lifetime of SOFC systems. Such a prediction should ideally be derivable from testing times shorter than the prerequisites for stationary SOFC application to minimize experimental efforts. The various parameters influencing MIC oxidation, e.g. environments with varying temperature, flow rates, gas compositions and $\text{H}_2\text{O}/\text{O}_2$ ratios affect both quantitatively and qualitatively the Cr_2O_3 microstructure. This unavoidably leads to a scatter in the scale thickness data (e.g. Fig. 5) and consequently requires an enlarged observation prediction interval (Figs. 6 and 7) for reliable information. Moreover, scale growth is shown in Figs. 8 and 11 to be driven by different oxidation mechanisms at different oxidation periods.

To get a reference for the investigation period needed for a reliable scale growth prediction we extrapolated some data fits according Eq. (2) based on data for a shorter test period e.g. for the heat treatment test we extrapolated the fitted scale growth function based on the scale thickness data for the first 1000 h. It turns out that for a statistically robust extrapolation the data should cover at least a quarter of the prediction interval which includes a sufficient amount of reliable data. Naturally for such an extrapolation the different overlaying mechanism during the initial stage (<500 h) has to be considered as well.

A direct transposition from the mean oxide scale thickness into ohmic losses needs furthermore an additional methodology. Such a method for the elaboration of ohmic resistances is currently under evaluation. It is based on the simulation of charge transport by using the finite element technique and it will include all the relevant microstructural information (variable scale thickness, local porosity etc.), which is described in the present paper. Furthermore with this modeling approach also the influence of variations in temperature and prevailing oxygen partial pressures on the intrinsic electrical conductivity of the oxide layers will be taken into account (see e.g. Ref. [56]). In this way we intend to obtain a complete picture of the relationships between (time dependent) scale thickness, microstructure, operating parameters and the resulting ohmic losses at the electrode-MIC interfaces.

5. Conclusions

In order to investigate Cr_2O_3 scale development on metallic interconnects, samples from stack tests up to 40,000 h as well as from heat treatment experiments were investigated. A systematic methodology for quantitative image analysis was applied to a large number of images from different sample locations. This approach allowed us to set up a database of oxide microstructures that comprises qualitative and quantitative scale characteristics for

different locations in the MICs and for a period, which covers the complete required SOFC lifetime for stationary applications.

Qualitative observations reveal a complex but systematic pattern of scale microstructures: On the cathode side the microstructures and scale thicknesses are relatively homogeneous. However the scales on the flats are slightly thicker than in the valleys. The interaction with the LSM protection layer leads to the formation of a conductive Mn-spinel within the oxide scale. In contrast, the scale growth on the anode side is thicker than on the cathode side and also more heterogeneous. The most important features of the scale microstructures on the anode side are the following: Scales on the flat are thicker than in the valley. In the center positions the interaction of the oxide layer with the Ni-mesh is more intense than in the outer positions. In the center and middle positions there is also a pronounced formation of Cr_2N , which is absent in the outer positions. In contrast, in the outer positions the scales contain a systematically higher porosity than in the center positions. No significant difference is observed between air inlet and gas flow fields.

Quantitative results are collected for scale thicknesses and associated growth rates up to 40,000 h. In the stack tests, the scale growth on the cathode side follows more or less a parabolic behavior ($n \approx 0.5$). In contrast, the scale growth on the anode side is better described with a non-parabolic law (Eq. (2)), where the exponential values are close to $n = 0.3$. These small n -values correspond with reduced scale growth during the long-term oxidation period. However, the rate constants k_e for the anode scales are higher than for the cathode scales, which explains the larger scale thicknesses for the anode.

The quantitative results from the exposure tests are comparable with data reported in literature. However the exposure tests show that the growth rates are dependent on material type. The scale development on industrial manufactured Crofer materials is enhanced in comparison to the CFY material, which can be attributed to impurities from manufacturing. Most important, in all our experiments a large scatter in the data points is observed at exposure times <1000 h. Only at longer exposure times (i.e. >1000 h) a steady state oxidation regime is reached which allows for a reliable determination of growth rates that are relevant for long-term predictions.

Overall, the observed variations of the scale microstructures, scale thicknesses and growth rates can be attributed to local variations of the influencing parameters (temperature, flow rate, pO_2 , pH_2O). The variation of parameters in the present work is associated with the systematic sampling of different location in the MIC. In order to understand the growth mechanism the MIC scales must be considered as dynamic systems, which involve different reaction steps. Thereby, the rate determining step for scale growth may change with time. Such a complex mechanism cannot be deduced entirely with a simple curve fit and extraction of a single exponential parameter. However, if the statistical basis includes a large number of samples and if it is collected over a sufficiently long observation period (i.e. 10,000 h), then the obtained growth rate allows for a reliable prediction of scale growth for the entire SOFC lifetime (40,000 h).

Future studies have to focus on the elaboration of the relationships between scale microstructure, scale thicknesses, growth rates and operating conditions with the corresponding resistances and ohmic losses at the MIC-electrode interface. For this purpose a dedicated finite element model is currently under development.

Acknowledgment

The authors wish to thank Swisselectric Research and the Swiss Federal Office of Energy SFOE for their financial support within the Swiss SOF-CH ESC project.

References

- [1] R. Steinberger-Wilckens, in: Proc. of the 12th International Symposium on Solid Oxide Fuel Cells XII (SOFC-XII), vol. 35, 2011, pp. 19–29.
- [2] A. Mai, B. Iwanschitz, R. Denzler, U. Weissen, D. Haberstock, V. Nerlich, A. Schuler, in: Proc. 10th European SOFC Forum A0403, 2012, pp. A0420–A0427.
- [3] K. Föger, in: Proc. 10th European SOFC Forum A0503, 2012, pp. A0518–A0524.
- [4] A. Nanjou, in: Proc. 10th European SOFC Forum 0202, 2012, p. A028.
- [5] A. Weber, E. Ivers-Tiffée, J. Power Sources 127 (2004) 273–283.
- [6] A. Buyukaksoy, V. Petrovksy, F. Dogan, ECS Trans. 45 (2012) 509–514.
- [7] Q. Ma, F. Tietz, A. Leonide, E. Ivers-Tiffée, Electrochim. Commun. 12 (2010) 1326–1328.
- [8] T. Armstrong, M. Smith, A. Virkar, Meeting Abstracts MA2005-01, 2006, p. 1155.
- [9] J. Wu, X. Liu, J. Mater. Sci. 26 (2010) 293–305.
- [10] Z. Yang, Int. Mater. Rev. 53 (2008) 39–54.
- [11] W. Quadakkers, J. Piron-Abellán, V. Shemet, L. Singheiser, Mater. High. Temp. 20 (2003) 115–127.
- [12] T. Richardson, Shreir's Corrosion, vol. 1, Elsevier Science, 2009.
- [13] Y. Larring, R. Haugsrød, T. Norby, J. Electrochem. Soc. 150 (2003) B374.
- [14] M. Stanislawski, J. Froitzheim, L. Niewolak, W. Quadakkers, K. Hilpert, T. Markus, L. Singheiser, J. Power Sources 164 (2007) 578–589.
- [15] P. Hou, J. Stringer, Mater. Sci. Eng. A 202 (1995) 1–10.
- [16] P. Kofstad, High Temperature Corrosion, Springer, 1988.
- [17] H.-P. Martinz, W. Köck, T. Sakaki, J. Phys. IV 03 (1993) C9-205–C9-213.
- [18] W. Zhu, S. Deevi, Mater. Sci. Eng. A 348 (2003) 227–243.
- [19] S. Fontana, R. Amendola, S. Chevalier, P. Piccardo, G. Caboche, M. Viviani, R. Molins, M. Sennour, J. Power Sources 171 (2007) 652–662.
- [20] Z. Lu, J. Zhu, E. Andrew Payzant, M.P. Paranthaman, J. Am. Ceram. Soc. 88 (2005) 1050–1053.
- [21] M. Stanislawski, E. Wessel, K. Hilpert, T. Markus, L. Singheiser, J. Electrochem. Soc. 154 (2007) A295.
- [22] S. Taniguchi, M. Kadokawa, H. Kawamura, T. Yasuo, Y. Akiyama, Y. Miyake, T. Saitoh, J. Power Sources 55 (1995) 73–79.
- [23] J.A. Schuler, P. Tanasini, A. Hessler-Wyser, C. Cominellis, J. Van herle, Electrochim. Commun. 12 (2010) 1682–1685.
- [24] W. Zhu, S. Deevi, Mater. Res. Bull. 38 (2003) 957–972.
- [25] N. Shaigan, W. Qu, D.G. Ivey, W. Chen, J. Power Sources 195 (2010) 1529–1542.
- [26] M. Linder, T. Hocker, R. Denzler, A. Mai, B. Iwanschitz, Fuel Cells 11 (2011) 573–580.
- [27] W.J. Quadakkers, Mater. Corros. 41 (1990) 659–668.
- [28] V. Sauchuk, S. Megel, E. Girdauskaite, N. Trofimenko, M. Kusnezoff, A. Michaelis, Russ. J. Electrochem. 47 (2011) 522–530.
- [29] M. Michalik, M. Hansel, J. Zurek, L. Singheiser, W.J. Quadakkers, Mater. High. Temp. 22 (2005) 213–221.
- [30] M. Palcut, L. Mikkelsen, K. Neufeld, M. Chen, R. Knibbe, P.V. Hendriksen, Corros. Sci. 52 (2010) 3309–3320.
- [31] W. Quadakkers, D. Naumenko, Oxid. Met. 61 (2004) 17–37.
- [32] D. Naumenko, B. Gleeson, E. Wessel, L. Singheiser, W. Quadakkers, Metall. Mater. Trans. A 38 (2007) 2974–2983.
- [33] X. Wang, F. Li, J. Chen, Y. Zhou, Corros. Sci. 58 (2012) 95–103.
- [34] H. Greiner, T. Grogler, W. Kock, in: 4th International Symposium on SOFC, 1995, pp. 879–888.
- [35] J. Fergus, Mater. Sci. Eng. A 397 (2005) 271–283.
- [36] K.P. Lillerud, J. Electrochem. Soc. 127 (1980) 2397.
- [37] P. Kofstad, in: Proc. 2nd European SOFC Forum, vol. 2, 1996, pp. 479–490.
- [38] D.M. Bastidas, Rev. Metal. Madrid 42 (2006) 425–443.
- [39] M. Hänsel, W. Quadakkers, D. Young, Oxid. Met. 59 (2003) 285–301.
- [40] H. Nickel, Y. Wouters, M. Thiele, W.J. Quadakkers, Anal. Bioanal. Chem. 361 (1998) 540–544.
- [41] J. Fergus, JOM – US 59 (2007) 56–62.
- [42] N. Birks, G.H. Meier, F.S. Pettit, in: Introduction to the High Temperature Oxidation of Metals, Cambridge University Press, 2006.
- [43] W. Quadakkers, H. Greiner, M. Hänsel, Solid State Ionics 91 (1996) 55–67.
- [44] E. Konysheva, U. Seeling, A. Besmehn, L. Singheiser, K. Hilpert, J. Mater. Sci. 42 (2007) 5778–5784.
- [45] J. Pirón Abellán, V. Shemet, F. Tietz, L. Singheiser, W. Quadakkers, in: Proc. of the 7th International Symposium on Solid Oxide Fuel Cells VII (SOFC-VII), vol. 16, 2001, pp. 811–819.
- [46] Z. Yang, G.-G. Xia, G.D. Maupin, J.W. Stevenson, J. Electrochem. Soc. 153 (2006) A1852–A1858.
- [47] E. Batawi, K. Honegger, R. Dietelhalm, M. Wetstein, in: Proc. 2nd European SOFC Forum, vol. 1, 1996, pp. 307–314.
- [48] Z. Yang, M. Walker, Electrochem. Solid State 6 (2003) 35–37.
- [49] Z. Yang, J.S. Hardy, M.S. Walker, G. Xia, S.P. Simner, J.W. Stevenson, J. Electrochem. Soc. 151 (2004) A1825.
- [50] P. Gannon, R. Amendola, JOM – US 64 (2012) 1470–1476.
- [51] K. Nakagawa, Y. Matsunaga, T. Yanagisawa, Mater. High. Temp. 20 (2003) 7.
- [52] H. Kurokawa, Y. Oyama, K. Kawamura, T. Maruyama, J. Electrochem. Soc. 151 (2004) A1264.
- [53] D.J. Young, High Temperature Oxidation and Corrosion of Metals, in: Corrosion Series, vol. 1, Elsevier Science, 2008.
- [54] P. Huczowski, N. Christiansen, V. Shemet, L. Niewolak, J. Piron-Abellán, L. Singheiser, W.J. Quadakkers, Fuel Cells 6 (2006) 93–99.
- [55] J. Froitzheim, Ferritic Steel Interconnectors and Their Interactions with Ni Base Anodes in Solid Oxide Fuel Cells (SOFC). Ph.D. thesis, RWTH Aachen, 2008.
- [56] J. Park, K. Natesan, Oxid. Met. 33 (1990).
- [57] ThyssenKrupp VDM GmbH, Crofer 22 APU, Material Data Sheet No. 4046, May Edition, 2010.
- [58] ThyssenKrupp VDM GmbH, Crofer 22 H, Material Data Sheet No. 4050, June Edition, 2010.
- [59] Plansee SE, Plansee SE, <http://www.plansee.com/en/Materials-Chromium-939.htm>, 2012.
- [60] P. Huczowski, Effect of Geometry and Composition of Cr Steels on Oxide Scale Properties Relevant for Interconnector Applications in Solid Oxide Fuel Cells (SOFCs). Ph.D. thesis, RWTH Aachen, 2005.